


## Convective Steady State in Shallow Cloud Fields

Tom Dror<sup>1</sup>, Ilan Koren<sup>1,\*</sup>, Huan Liu<sup>1</sup>, and Orit Altaratz<sup>1</sup>

*Department of Earth and Planetary Sciences, Weizmann Institute of Science, Rehovot 7610001, Israel*

 (Received 6 February 2023; revised 22 June 2023; accepted 29 August 2023; published 27 September 2023)

Shallow cloud fields exhibit different patterns, such as closed or open hexagonal cells and cloud streets. These patterns play a key role in determining the cloud fields' radiative effects, thereby affecting the climate. Here, we show that a large subset of shallow cloud fields forms organized, mesoscale-sized, regular patterns that persist for extended times. It emanates from the steady state of the underlying rigid configuration of convection cells. From a climate perspective, in a sea of cloud complexity, the convective steady-state provides an "island of simplicity." The convective steady state can be parametrized in climate models to better capture the feedback of such cloud fields in a warming climate.

DOI: [10.1103/PhysRevLett.131.134201](https://doi.org/10.1103/PhysRevLett.131.134201)

Shallow cloud fields cover large areas over the world's oceans and lands. They reflect part of the shortwave radiation while emitting in the long wave at a temperature close to that of Earth's surface, thus contributing to a net cooling effect on the planet [1]. We still lack a full understanding of the interplay between the governing processes that control shallow cloud fields' properties and their feedback to changes in environmental conditions. Consequently, the representation of such fields in climate models leads to large uncertainties in climate predictions [1,2].

Shallow cloud fields were shown to exhibit a variety of patterns, such as closed or open hexagonal cells [3–5], cloud streets [6], clusters [7,8], skeletal networks, or mesoscale arcs [9]. Such patterns are often referred to as the cloud field's organization. The organization derives from the interaction of numerous processes related to the internal dynamical and microphysical cloud processes and the large-scale external forcing dictated by meteorological conditions. The field's organization affects and is affected by environmental conditions and plays a key role in determining its properties. It can affect the clouds' sizes, lifetimes, and precipitation patterns and, hence, the overall radiative effects [10].

A conceptual model describing the interplay between cloud formation by condensation and depletion by rain based on the properties of marine stratocumulus clouds (MSCs) demonstrated a solution space with two nonchaotic states: steady state and nonharmonic oscillations [11]. A simplified version of the model expressed as a first-order nonlinear delay differential equation describes how the time-dependent cloud depth ( $H$ ) is controlled by the aerosol concentration ( $N$ ), which regulates the strength of the sink term (rain) [12]:

$$\frac{dH}{dt} = \frac{H_0 - H}{\tau} - \frac{\alpha}{\sqrt{N}} H^2(t - D), \quad (1)$$

Here  $H_0$  is the cloud carrying capacity representing the thermodynamic conditions (instability) by means of the system's maximal potential for cloud depth,  $\tau$  is the characteristic time for reaching the carrying capacity (i.e., the cloud recovery time),  $\alpha$  is a scaling constant ( $\sim 100 \text{ day}^{-1} \text{ m}^{-2.5}$ ) determined by theoretical considerations and measurements [13–15],  $D$  is the time delay of the sink term, representing the time of conversion of droplets to rain by stochastic microphysical collection processes, and  $t$  is time.

The steady-state solution ( $dH/dt = 0$ ) reflects a balance between cloud-forming and cloud-depleting processes; i.e., light rain consumes the cloud at the exact rate of cloud replenishment. A Hopf bifurcation separates the steady state from an oscillating state, which describes processes of cloud formation by environmental instability and condensation and cloud depletion [12,16]. Observations show that the oscillatory solution is captured in the morphology of open cells [17]. Open cells precipitate and oscillate; their patterns change over time as the clouds form, rain, and deplete [11,18,19]. The steady-state solution represents closed cells in MSCs. It results in a rigid cloud field structure, composed of many such closed cells, which lasts for several days, creating cloud decks that extend to thousands of kilometers over the eastern subtropical oceans [4]. However rigid, convective steady state (CSS) does not imply stagnation. It suggests a dynamical, Rayleigh-Bénard-convection-like balance for which the Rayleigh number exceeds the critical threshold to initiate organized convection. Still, it is small enough to dictate steady convective cells that occupy the entire field [20,21]. The CSS is reflected both in the spatial and temporal domains. It manifests as uniformly organized patterns with a strong tendency toward regularity (cellular, grid, or linear) [7,22].

Many works were dedicated to studying the oscillations in open cells, e.g., [12,18,19], while less attention was given to the steady-state regime. In this work, we expand

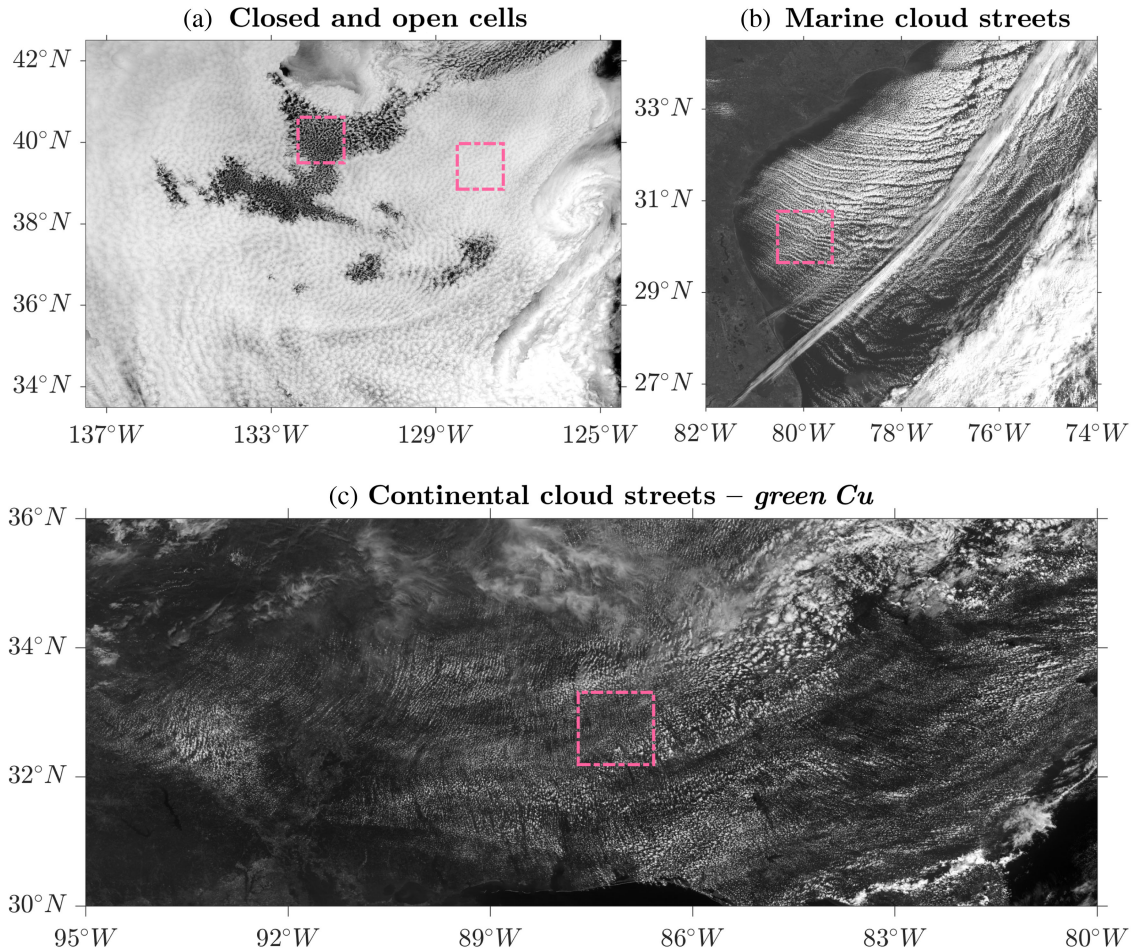


FIG. 1. Gallery of patterns formed by shallow cloud fields. Corrected reflectance ( $R$ ) images of (a) closed cells and pockets of open cells in MSCs captured over the northeastern Pacific Ocean on April 10, 2020. (b) Cloud streets along the east coast of the United States on December 1, 2020. (c) Cloud streets formed by green cumulus clouds over the continental United States on August 22, 2018. Images obtained by NOAA’s GOES-16 and GOES-17 satellites [27]. The areas where Lagrangian tracking was initiated are marked by the dashed boxes.

the concept of CSS to other boundary-layer clouds that exhibit high regularity in their organization, such as cloud streets over ocean and land (Fig. 1). Cloud streets appear over both water and land as individual shallow cumulus clouds are organized by horizontal roll vortices during cold air outbreaks over the sea or in the daytime planetary boundary layer (PBL) over land [6,23]. Continental cloud streets consist of shallow cumuli that line up as pearls on a string. These continental clouds, recently termed *green cumulus* due to their tendency to form over forested and vegetated regions [24], are distinguished by their strict regular organization [24,25], forming either grid or cloud street mesoscale patterns that may persist over the course of a day [26].

To examine the morphological evolution of shallow cloud fields, we use the high spatiotemporal resolution of the GOES satellite dataset [28], and the Weather Research and Forecasting (WRF) modeling data [29]. The satellite dataset consists of images of visible

reflectance ( $0.64\ \mu\text{m}$ ) obtained every 5 minutes at a fine resolution of  $0.5\ \text{km}$  from the Advanced Baseline Imager onboard GOES-17 and GOES-16. The simulations dataset includes the mean vertical velocity of the lower PBL ( $\bar{w}$ -field). The  $\bar{w}$ -field’s resolution depends on the simulation (between 222 and 600 m and 1–2 sec; see Fig. S1 and Table S1 in Supplemental Material [30]). We use a Lagrangian framework, relying on a tracking approach first introduced by [17], to track patterns of corrected reflectance ( $R$ ) and  $\bar{w}$ , representing the clouds and the underlying convective cells as indicators of the field’s organization. The Lagrangian framework corrects for the mean flow (i.e., advection) and allows a detailed view of the secondary flow, reflecting the organization’s nature [6]. For further information on datasets and Lagrangian tracking, refer to the Supplemental Material [30] and Appendix A, respectively.

Following the same cloud element provides insights regarding the convective cells’ local morphology and time

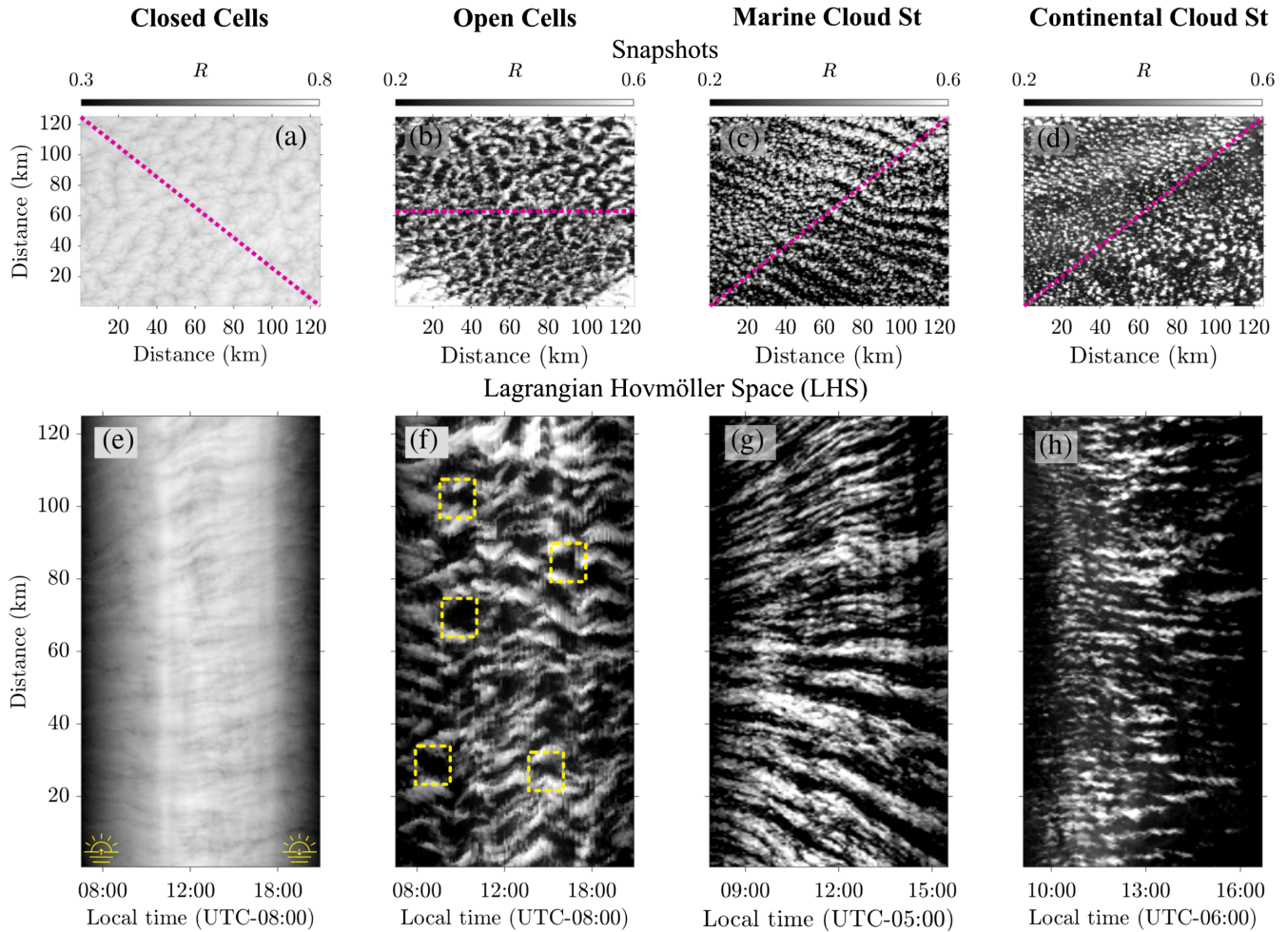


FIG. 2. Lagrangian analysis observations. Snapshots of tracked  $R$  boxes of (a) closed and (b) open cells, (c) marine cloud streets, and (d) continental cloud streets (green cumulus). The dashed magenta lines mark the cross section used to form the LHS. Below each snapshot, the corresponding LHS is shown (e)–(h). Dashed yellow polygons in (f) mark areas of cloud segments splitting due to rain.

evolution. Thus, if the patterns last for a significant part of the day, the corresponding Lagrangian corrected dataset will maintain a similar structure [17,19,31]. This is clearly demonstrated in Video S1 in Ref. [32], showing that the patterns of the Lagrangian-corrected  $\bar{w}$ -fields are quasistationary in time.

Following the Lagrangian correction, we form the Lagrangian-Hovmöller space (LHS), which indicates how close the system is to a CSS. The LHS is obtained by extracting a cross section from each Lagrangian-corrected snapshot and stacking them into a matrix. In the LHS matrix, the axis parallel to the extracted cross sections reflects the spatial dimension, while the orthogonal axis is the time. If the Lagrangian tracking successfully corrects for the mean flow and the system is in a CSS, the corresponding LHS will map convective elements as straight lines parallel to the time axis. Apart from theoretical cases unlikely to occur in nature, such mapping is unique; i.e., the long parallel lines will appear *only* if the

two conditions are satisfied (more details regarding the formulation of the LHS are found in Appendix B and in the Supplemental Material [31]).

Starting with observations, we track  $125 \text{ km}^2$  representative boxes for 11 h in the case of open and closed cells and  $\sim 7:45$  h in the case of marine and continental cloud streets (see the boxes in Fig. 1 and snapshots of the boxes in Fig. 2).

For each box, we extract a Lagrangian cross section of  $R$  [17,19], form the LHS, and evaluate the CSS. As expected, the closed cells maintain an approximately fixed spatial structure, and the diurnal cycle of  $R$  contains almost all the variability. The straight ridges in Fig. 2(e) elucidate that the closed cells do not exhibit significant structural changes during the analysis. Analogous to the closed cells, the LHS of the marine cloud streets exhibits horizontal patterns [Fig. 2(g)]. The patterns are perfectly horizontal in the center of the matrix but diverge above (tilt upward) and below (tilt downward) the center. The divergence of the

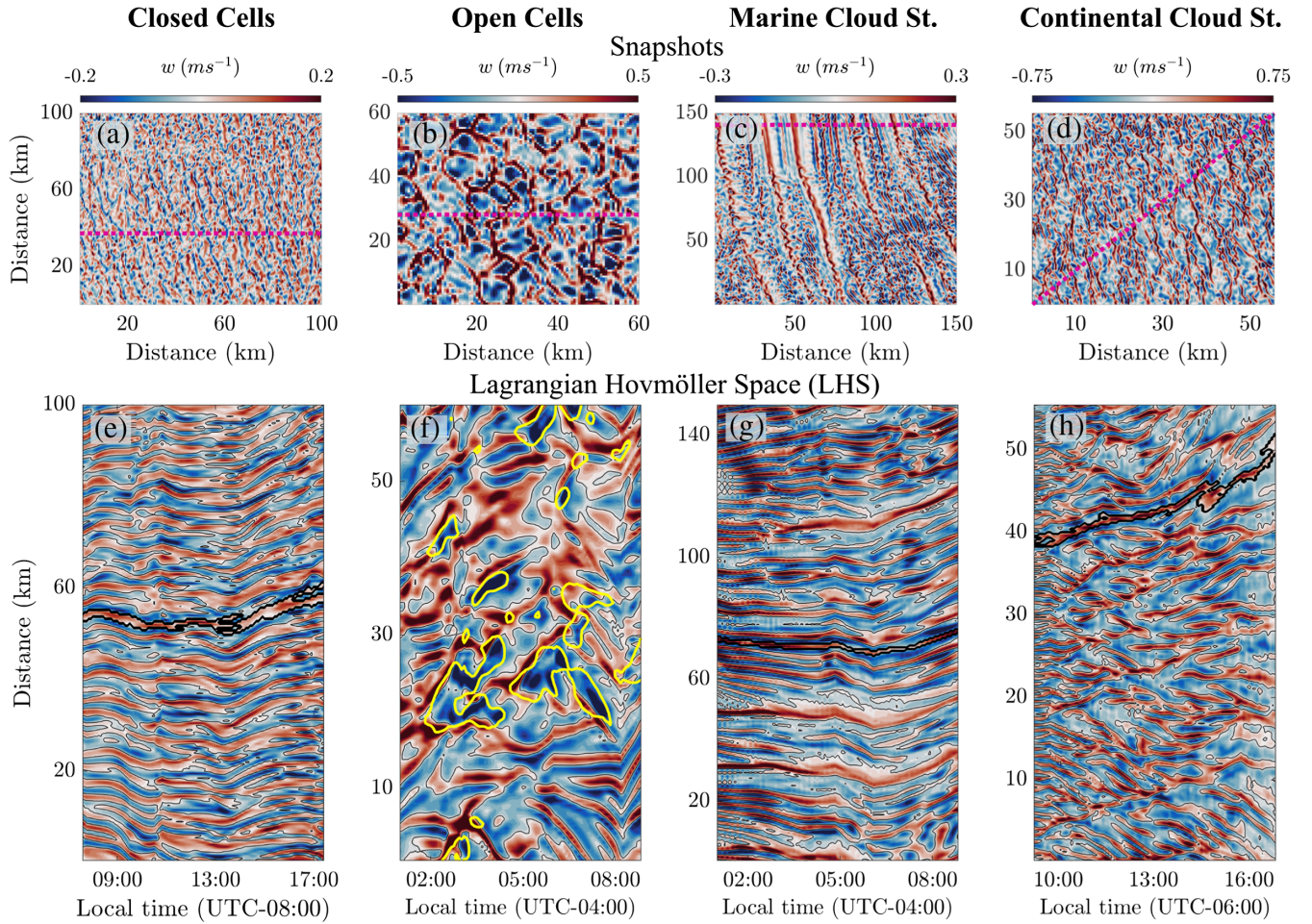


FIG. 3. Lagrangian analysis modeling. Snapshots of the tracked  $\bar{w}$  boxes of (a) closed and (b) open cells and (c) marine and (d) continental cloud streets. The dashed magenta lines mark the cross sections used to form the LHS. Below each snapshot, the corresponding LHS are shown (e)–(h). In panels (e), (g), and (h), thick black contours delineate the horizontal extent of positive updraft objects, while the yellow contour in (f) marks areas with substantial rain below the cloud base (rainwater path  $> 6 \text{ gm}^{-2}$ ).

patterns indicates the mean flow is not uniform within the selected box, such that the upper and lower parts of the box are likely subjected to a slightly different advection.

The elongated stripes in the green cumulus LHS [Fig. 2(h)] are less coherent than in the closed cells. Unlike the ocean, the land surface is heterogeneous, exhibiting variations in land cover, terrain roughness, and topography. These irregularities act as perturbations to the CSS, resulting in changes and meandering of the continental cloud street patterns. Nonetheless, the green cumulus LHS exhibits straight patterns parallel to the time axis that persist for periods of up to five hours.

The LHS of the open cells shows a different pattern. The segments are short and often discontinuous. That is, many segments end in a triple-junction structure in which they split into two parts, above and below it [see yellow dashed boxes in Fig. 2(f)].

The top-down nature of satellite observations is limited in its ability to inform us regarding the flow in PBL. In that respect, clouds serve as markers for convection

organization. We argue that the CSS is a quantity related to the essence of convection and refer to the convection cells as the preserved entity. Note that in Eq. (1) the term  $(dH/dt)$  (the change of cloud depth with time) essentially corresponds to the vertical velocity ( $w$ ). Thus, and to further explore the CSS assumption, we employ a cloud-resolving model able to produce the otherwise invisible pattern of updrafts and downdrafts shaping the cloud field's organization.

We have simulated fields of closed and open cells and marine and continental cloud streets using the WRF model (see Supplemental Material and Fig. S1 [30]). The simulations were able to capture the cloud field patterns with a remarkable similarity to observations (Fig. 5), which strengthens our confidence in the ability of the model to capture the governing processes determining the fields' organization. We follow the  $\bar{w}$ -field, which explicitly represents the structure of convection cells.

Consistently with the analysis of the observational dataset, we track the boxes of different cloud fields, now

in the  $\bar{w}$  domain. We subsequently follow their evolution during  $\sim 10$  h for the closed cells and  $\sim 8$  h for the open cells and the cloud street fields. See characteristic snapshots of the boxes in the upper row of Fig. 3 and the boxes' time evolution in video S1 [30].

Starting with the nonprecipitating or lightly precipitating cloud fields, the  $\bar{w}$ -LHS of the simulated closed cells [Fig. 3(e)] and of both marine and continental streets [Figs. 3(g) and 3(h)] exhibit mostly an uninterrupted horizontal linear pattern. The marine cloud fields show updraft segments that remain remarkably steady throughout the simulations' time. The LHS of the continental cloud streets exhibits a noisier manifestation of the aforementioned horizontal patterns. Recall that the green cumulus field is subject to larger environmental variations, such as surface heterogeneity and a strong diurnal cycle. For example, the green cumulus box passes over different topographies throughout the day (Fig. S2 [30]). These variations induce a slow drift of the green cumulus patterns during the day, observed in the simulation. Nonetheless, continuous *nearly* horizontal updraft segments persist for several hours, and some even remain for the entire simulation duration ( $\sim 8$  h).

The  $\bar{w}$ -LHS of the simulated open cells shows the recharge-discharge patterns associated with the oscillatory solution of Eq. (1); updraft segments abruptly break when significant rain falls [Fig. 3(f); see also Fig. S3 [30]]. Induced downdrafts, fueled by rain evaporation below the cloud base, counteract the updrafts, often reversing the flow such that the updrafts at the core of the convective cells are shifted to the sides. Such an effect is manifested by a triple-junction pattern, similar to that obtained by the observations. The yellow contour in Fig. 3(f) (marking rainwater path  $> 6 \text{ g m}^{-2}$ ) lies perfectly on the triple junctions, where convection cells perish and split to form the new generation of clouds.

For the theoretical steady state, obtained when the right-hand side of Eq. (1) equals zero ( $dH/dt = 0$ ), convection cells are expected to last forever. In nature, however, the averaged spatial scale ( $L$ ) of an atmospheric phenomenon is typically proportional to its averaged timescale ( $T$ ), such that  $T \propto L^{2/3}$  [33–36]. The emergence of a CSS breaks this time-space scaling. An  $\mathcal{O}(10 \text{ km})$  closed cell in MSC, and an  $\mathcal{O}(1 \text{ km})$  shallow cumulus over the ocean, and green cumulus over land, form highly organized mesoscale-sized patterns that last longer than predicted. Using the LHS we estimate a characteristic lifetime for convective cells in the different simulated cloud fields. We define positive updraft objects and examine their horizontal extent; see, e.g., highlighted objects in Figs. 3(e), 3(g), and 3(h). In the absence of significant rain, the characteristic lifetime of many of the convective cells over the ocean spans the whole simulation time. In the case of the continental cloud streets, surface fluxes inhomogeneities driven by changes in the topography and surface properties (such as vegetation type and water bodies) perturb the flow, causing the convective

cells to meander or even break. Nevertheless, the lifetime of many of the continental convective segments spans a few hours (more than half of the simulation time). Considering the typical spatial scale of the convective cells, as determined from both observation and model data, we use the ratio between the observed and the expected lifetime to estimate the CSS signature on the field:

$$\sigma = \frac{T_{\text{observed}}}{T_{\text{expected}}} \quad (2)$$

We estimate  $\sigma > 75$  for the closed cells,  $\sigma > 280$  for marine cloud streets, and  $\sigma > 144$  for continental cloud streets. Note that the  $\sigma$  values of the marine cloud fields are lower-bound estimations. The cells might endure even longer. However, our analysis is limited to visible wavelengths during the daytime. Moreover, cloud fields are advected throughout different environmental and aerosol conditions that together with the diurnal cycle break the symmetry and act as perturbations to the CSS. Thus,  $T_{\text{observed}}$  is limited to temporal scales of a few days over the ocean and several hours over the continents, where the stronger diurnal cycle dictates faster thermodynamic changes. Still, for all cases shown here  $\sigma \gg 1$ , suggesting that self-organization processes act to prolong the lifetime of convection cells toward the cloud field's characteristic scales ( $L \sim 1000 \text{ km}$ ,  $T \sim 24 \text{ h}$ ).

Shallow convective cloud fields form mesoscale patterns that are largely ignored in climate models. This can be traced back to the insufficient understanding of mesoscale organizing processes and their impacts on larger scales. Specifically, the radiative impact of such cloud patterns is not completely understood. By combining observations and simulations, this work bridges the gap between theory and practice and between the convection cell scale to the mesoscale and enhances our understanding of cloud pattern formation and the patterns' stability over time. The CSS can be used as a first approximation when parametrizing shallow cloud fields. Perturbations driven by the onset of rain or by changes in the surface properties could then be introduced to push the fields away from equilibrium. The CSS provides an "island of simplicity" in highly complex cloudy systems and is likely to better capture their lifetimes and extents, and therefore their radiative properties. Moreover, such an understanding will yield a better comprehension of shallow cloud feedback to global warming. The question of how the CSS will respond to changes in the meteorological conditions within a warming climate remains, however, open.

All satellite data used in this study are publicly available from NOAA [37] (GOES-R data) and NASA [38] (NASA true-color images). All the Lagrangian-corrected data used in this study, including a video showing the time evolution of the  $\bar{w}$ -field patterns associated with the different cloud

fields, as well as the code used to form the LHS, are available in an online repository Ref. [32].

This research received funding from the European Research Council (ERC) under the European Union’s Horizon 2020 research and innovation programme (Grant Agreement No. 810370). We thank three anonymous reviewers, whose comments have improved the manuscript considerably.

The authors declare that there are no competing interests.

*Appendix A: Lagrangian analysis*—The high spatio-temporal resolution of both the satellite and the model simulation datasets enables us to accurately track the different boxes as they are advected by the wind and examine their time evolution using a Lagrangian framework, as introduced by [17]. The high resolution is critical for the success of the Lagrangian tracking since we target fine convective elements and determine their optimal displacement based on the fact that the characteristic time of the patterns’ morphological changes is much longer than the sampling rate. In short, the tracking algorithm detects shifting caused by advection by utilizing the fact that local patterns in the cloud field evolve slower than the sampling rate (15 min in [17], 5 min in this study). Thus, the mean flow (advection) can be determined by optimizing the similarity between two consecutive images. In the case of the satellite dataset, we track the evolution of clouds by tracking the corrected-reflectance ( $R$ ) signal, and in the modeling simulation dataset, we track the mean vertical wind in the PBL  $\bar{w}$ -field, obtained by averaging the vertical velocity ( $w$ ) between the second vertical level to that corresponding to the averaged cloud base height. See examples of the time evolution of the Lagrangian-corrected  $\bar{w}$ -fields in Video S1 [32]. The video shows that the convection cells’ pattern associated with the different simulated cloud fields is quasistationary in time, illustrating successful advection correction. We note that the changing topography and land cover (over land), winds, and different surface temperatures affect cloud fields drifted by winds. Therefore, the steady-state fields’ manifold could undergo affine transformations, exhibiting stretching, rotations, and local deformations. The deformations are seen in the video as the slight movements and drifting of the tracked patterns.

*Appendix B: Synthetic data analysis and LHS mapping*—We demonstrate the convective steady-state manifestation and the mapping to the Lagrangian-Hovmöller space using synthetic data that reflect the cloud or vertical velocity patterns associated with different cloud fields, namely closed cells, open cells, and cloud streets [Figs. 4(a)–4(c)]. In this synthetic scenario, a successful Lagrangian correction of a field in CSS results in an

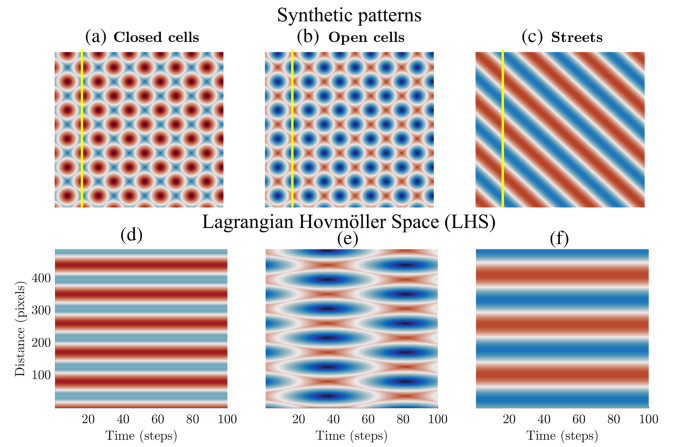


FIG. 4. Synthetic data. Artificially produced ( $491 \times 491$  pixels) patterns of (a) closed cells, (b) open cells, and (c) linear streets. The resulting Lagrangian-Hovmöller space (LHS), generated by tracing along the yellow line within each Lagrangian-corrected frame, is depicted below each pattern (d)–(f).

unchanging frame seen at all times. By selecting a vertical trace from the same location in each Lagrangian-corrected frame [e.g., the  $n$ th vertical trace, as indicated by the yellow vertical line in Figs. 4(a)–4(c)] and stacking them to create the LHS, a repetitive trace along the (horizontal) time axis emerges. If the trace holds a structural pattern (e.g., it crosses several convective cells), this structure becomes frozen and displayed as straight lines parallel to the time axis [Figs. 4(d) and 4(f)]. However, consider a synthetic oscillating case where the first frame consists of convective cells forming over the nodes of a square grid, while the grid centers remain empty. As time progresses, the cells dissipate while new ones form in the grid centers, and then they dissipate and new cells form in the nodes, completing an oscillation cycle with a period  $\tau$ . Defining the satellite sampling rate as  $t$ , when  $\tau \gg t$ , the Lagrangian tracking method effectively corrects for advection. Thus, a sequence of Lagrangian-corrected frames will display stationary oscillating cells, transitioning between nodes and centers. Assuming the initial frame’s  $n$ th vertical trace crosses nodes and surrounding cells, after half a period, it will encounter no convective cells, ultimately aligning with the first trace after another half period. Consequently, the LHS showcases steady oscillations of tracers mirroring the cells’ temporal evolution [Fig. 4(e)]. Further insights into the generation of synthetic patterns and the mathematical framework of the LHS are provided in the Supplemental Material [30].

*Appendix C: Cloud pattern comparison: Observations versus simulations*—We conducted a comparison between observed and simulated cloud patterns to validate the accuracy of the model. Figure 5 clearly shows that the

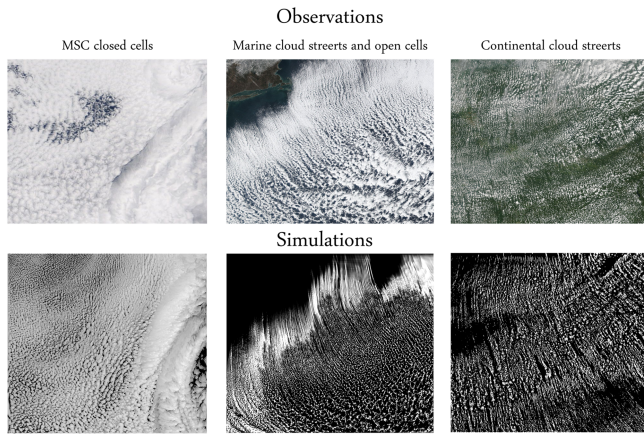


FIG. 5. Observed versus simulated cloud patterns. Observed (upper row) versus simulated (lower row) patterns of closed cells in MSC clouds over the northeastern Pacific Ocean on April 10, 2020. Marine cloud streets followed by open cells downwind over the northwestern Atlantic Ocean on January 17, 2020 and continental cloud streets formed by green cumulus over the central United States on August 22, 2018 (columnwise, from left to right). Observations show “true-color” images taken by MODIS Aqua, VIIRS Soumi-NPP, and MODIS Terra for closed cells, marine cloud streets together with open cells, and continental cloud streets, respectively. We acknowledge the use of imagery from the NASA Worldview application [38], part of the NASA Earth Observing System Data and Information System (EOSDIS). Simulated images show the cloud water path.

simulated cloud patterns closely resemble the observed ones, reinforcing our confidence in the model’s capability to accurately capture the underlying processes governing the organization of the fields.

\*ilan.koren@weizmann.ac.il

- [1] P. Forster, T. Storelvmo, K. Armour, W. Collins, J.-L. Dufresne, D. Frame, D. Lunt, T. Mauritsen, M. Palmer, M. Watanabe, M. Wild, and H. Zhang, The earth’s energy budget, climate feedbacks, and climate sensitivity, in *Climate Change 2021: The Physical Science Basis. Contribution of Working Group I to the Sixth Assessment Report of the Intergovernmental Panel on Climate Change*, edited by V. Masson-Delmotte, P. Zhai, A. Pirani, S. Connors, C. Péan, S. Berger, N. Caud, Y. Chen, L. Goldfarb, M. Gomis, M. Huang, K. Leitzell, E. Lonnoy, J. Matthews, T. Maycock, T. Waterfield, O. Yelekçi, R. Yu, and B. Zhou (Cambridge University Press, Cambridge, England, 2021), pp. 923–1054.
- [2] M. D. Zelinka, T. A. Myers, D. T. McCoy, S. Po-Chedley, P. M. Caldwell, P. Ceppi, S. A. Klein, and K. E. Taylor, Causes of higher climate sensitivity in CMIP6 models, *Geophys. Res. Lett.* **47**, e2019GL085782 (2020).
- [3] R. Wood and C. S. Bretherton, On the relationship between stratiform low cloud cover and lower-tropospheric stability, *J. Clim.* **19**, 6425 (2006).
- [4] D. Rosenfeld, Y. Kaufman, and I. Koren, Switching cloud cover and dynamical regimes from open to closed Benard cells in response to the suppression of precipitation by aerosols, *Atmos. Chem. Phys.* **6**, 2503 (2006).
- [5] F. Glassmeier and G. Feingold, Network approach to patterns in stratocumulus clouds, *Proc. Natl. Acad. Sci. U.S.A.* **114**, 10578 (2017).
- [6] R. A. Brown, Longitudinal instabilities and secondary flows in the planetary boundary layer: A review, *Rev. Geophys.* **18**, 683 (1980).
- [7] T. Zhu, J. Lee, R. Weger, and R. Welch, Clustering, randomness, and regularity in cloud fields: 2. Cumulus cloud fields, *J. Geophys. Res.* **97**, 20537 (1992).
- [8] T. Heus and A. Seifert, Automated tracking of shallow cumulus clouds in large domain, long duration large eddy simulations, *Geosci. Model Dev.* **6**, 1261 (2013).
- [9] B. Stevens, S. Bony, H. Brogniez, L. Hentgen, C. Hohenegger, C. Kiemle, T. S. L’Ecuyer, A. K. Naumann, H. Schulz, P. A. Siebesma *et al.*, Sugar, gravel, fish and flowers: Mesoscale cloud patterns in the trade winds, *Q. J. R. Meteorol. Soc.* **146**, 141 (2019).
- [10] I. Tobin, S. Bony, and R. Roca, Observational evidence for relationships between the degree of aggregation of deep convection, water vapor, surface fluxes, and radiation, *J. Clim.* **25**, 6885 (2012).
- [11] I. Koren and G. Feingold, Aerosol–cloud–precipitation system as a predator-prey problem, *Proc. Natl. Acad. Sci. U.S.A.* **108**, 12227 (2011).
- [12] I. Koren, E. Tziperman, and G. Feingold, Exploring the nonlinear cloud and rain equation, *Chaos* **27**, 013107 (2017).
- [13] A. Kostinski, Drizzle rates versus cloud depths for marine stratocumuli, *Environ. Res. Lett.* **3**, 045019 (2008).
- [14] M. VanZanten, B. Stevens, G. Vali, and D. Lenschow, Observations of drizzle in nocturnal marine stratocumulus, *J. Atmos. Sci.* **62**, 88 (2005).
- [15] H. Pawlowska and J.-L. Brenguier, An observational study of drizzle formation in stratocumulus clouds for general circulation model (GCM) parameterizations, *J. Geophys. Res.* **108** (2003).
- [16] M. D. Chekroun, I. Koren, and H. Liu, Efficient reduction for diagnosing Hopf bifurcation in delay differential systems: Applications to cloud-rain models, *Chaos* **30**, 053130 (2020).
- [17] I. Koren and G. Feingold, Adaptive behavior of marine cellular clouds, *Sci. Rep.* **3**, 2507 (2013).
- [18] G. Feingold, I. Koren, H. Wang, H. Xue, and W. A. Brewer, Precipitation-generated oscillations in open cellular cloud fields, *Nature (London)* **466**, 849 (2010).
- [19] H. Liu, I. Koren, O. Altaratz, R. H. Heiblum, P. Khain, X. Ouyang, and J. Guo, Oscillations in deep-open-cells during winter mediterranean cyclones, *npj Clim. Atmos. Sci.* **4**, 12 (2021).
- [20] A. Pandey, J. D. Scheel, and J. Schumacher, Turbulent superstructures in Rayleigh-Bénard convection, *Nat. Commun.* **9**, 2118 (2018).
- [21] B. Zhou, J. S. Simon, and F. K. Chow, The convective boundary layer in the terra incognita, *J. Atmos. Sci.* **71**, 2545 (2014).

- [22] R. Weger, J. Lee, T. Zhu, and R. Welch, Clustering, randomness and regularity in cloud fields: 1. Theoretical considerations, *J. Geophys. Res.* **97**, 20519 (1992).
- [23] D. Etling and R. Brown, Roll vortices in the planetary boundary layer: A review, *Bound.-Lay. Meteorol.* **65**, 215 (1993).
- [24] T. Dror, I. Koren, O. Altaratz, and R. H. Heiblum, On the abundance and common properties of continental, organized shallow (green) clouds, *IEEE Trans. Geosci. Remote Sens.* **59**, 4570 (2020).
- [25] T. Dror, V. Silverman, O. Altaratz, M. D. Chekroun, and I. Koren, Uncovering the large-scale meteorology that drives continental, shallow, green cumulus through supervised classification, *Geophys. Res. Lett.* **49**, e2021GL096684 (2022).
- [26] T. Dror, M. D. Chekroun, O. Altaratz, and I. Koren, Deciphering organization of GOES-16 green cumulus through the empirical orthogonal function (EOF) lens, *Atmos. Chem. Phys.* **21**, 12261 (2021).
- [27] G.-R. C. W. Group *et al.*, NOAA GOES-R series advanced baseline imager (ABI) level 1b radiances (2017).
- [28] T. J. Schmit, P. Griffith, M. M. Gunshor, J. M. Daniels, S. J. Goodman, and W. J. Lebar, A closer look at the ABI on the GOES-R series, *Bull. Am. Meteorol. Soc.* **98**, 681 (2017).
- [29] W. C. Skamarock, J. B. Klemp, J. Dudhia, D. O. Gill, Z. Liu, J. Berner, W. Wang, J. G. Powers, M. G. Duda, D. M. Barker *et al.*, *A Description of the Advanced Research WRF Model Version 4.3* (National Center for Atmospheric Research: Boulder, CO, 2021).
- [30] See Supplemental Material at <http://link.aps.org/supplemental/10.1103/PhysRevLett.131.134201> for additional figures and exploitations on satellite observations, model simulations, synthetic data, and the mathematical formulation of LHS, as well as on the green cumulus topography and rain LHS.
- [31] A. Gufan, Y. Lehahn, E. Fredj, C. Price, R. Kurchin, and I. Koren, Segmentation and tracking of marine cellular clouds observed by geostationary satellites, *Int. J. Remote Sens.* **37**, 1055 (2016).
- [32] T. Dror-Schwartz, I. Koren, H. Liu, and O. A. Stollar, Data from: Convective steady-state in shallow cloud fields, [10.34933/wis.000653](https://doi.org/10.34933/wis.000653).
- [33] P. B. Chilson, W. F. Frick, J. F. Kelly, K. W. Howard, R. P. Larkin, R. H. Diehl, J. K. Westbrook, T. A. Kelly, and T. H. Kunz, Partly cloudy with a chance of migration: Weather, radars, and aerocology, *Bull. Am. Meteorol. Soc.* **93**, 669 (2012).
- [34] K. Sene, Meteorological forecasting, in *Hydrometeorology: Forecasting and Applications* (Springer International Publishing, Cham, Switzerland, 2016), pp. 105–140.
- [35] J. Smagorinsky, Global atmospheric modeling and the numerical simulation of climate, *Weather Clim. Modification*, 633 (1974).
- [36] M. Cullen, Modelling atmospheric flows, *Acta Numer.* **16**, 67 (2007).
- [37] <https://www.ngdc.noaa.gov/>.
- [38] <https://worldview.earthdata.nasa.gov/>.